Journal of
Water & Climate Change

IWA PUBLISHING

Journal of Water and Climate Change Vol 13 No 2, 926 doi: 10.2166/wcc.2021.432

An estimation of the evapotranspiration of typical steppe areas using Landsat images and the METRIC model

Jun Wang[a,b,*], Heping Li[a,b] and Haiyuan Lu[a,b]

[a] Yinshanbeilu Grassland Eco-hydrology National Observation and Research Station, China Institute of Water Resources and Hydropower Research, Beijing 100038, China
[b] China Institute of Water Resources and Hydropower Research, Institute of Water Resources for Pastoral Area, Hohhot 010020, China
*Corresponding author. E-mail: slwj1988@163.com

ABSTRACT

Remote sensing excels in estimating regional evapotranspiration (ET). However, most remote sensing energy balance models require researchers to subjectively extract the characteristic parameters of the dry and wet limits of the underlying surfaces. The regional ET accuracy is affected by wrong determined ideal pixels. This study used Landsat images and the METRIC model to evaluate the effects of different dry and wet pixel combinations on the ET in the typical steppe areas. The ET spatiotemporal changes of the different land cover types were discussed. The results show that the surface temperature and leaf area index could determine the dry and wet limits recognition schemes in grassland areas. The water vapor flux data of an eddy covariance system verified that the relative error between the $ET_{d,METRIC}$ and $ET_{d,GES}$ of eight DOY_s (day of the year) was 18.8% on average. The ET_{METRIC} values of the crop growth season and the ET_{IMS} of eight silage maize irrigation monitoring stations were found to have a relative error of 11.1% on average. The spatial distribution of the ET of the different land cover types in the study area was as follows: $ET_{water} > ET_{arable\ land} > ET_{forest\ land} > ET_{unutilized\ land} > ET_{grassland} > ET_{urban\ land}$.

Key words: dry and wet limits, evapotranspiration, METRIC model, remote sensing, typical steppe areas

HIGHLIGHTS

- Landsat images and the METRIC model estimating regional ET had obtained reliable and accurate results in typical steppe areas.
- The water vapor flux data of an eddy covariance system conducted the verification.
- The surface temperature and leaf area index could determine the dry and wet limits recognition schemes in grassland areas.

1. INTRODUCTION

Steppe ecoregions are important natural resources in northern China, and are mainly distributed in the semi-arid regions of Eurasia where the vast majority of the rivers are seasonal inland rivers (Batnasan 2003; Tong *et al.* 2004). Due to this hydrogeographical feature, it can be expected that the precipitated water will result in only minimal discharges to the rivers or ground water. For example, the water exchange between the grassland areas and the atmosphere through precipitation and evapotranspiration (ET) will be the main branch of the hydrological cycle in steppe environments (Yamanaka *et al.* 2007). In recent years, large-scale human activities have changed the gall atmosphere, surfaces, soil, and underground processes of the natural water cycle, which had led to the hydrologic cycles presenting obvious 'natural-artificial' dual properties in the modern environmental settings (Wang *et al.* 2006). ET is an important component of the prairie hydrologic cycles (Allen *et al.* 1998). When the ET is disturbed, the results will cause changes in the regional hydrological balances, which may have major impacts on the regional water storage processes (Bradley 1999). Therefore, the accurate estimations of the ET in grassland areas are of great significance to hydrological process change simulations and water resource management decision-making, as well as grassland drought monitoring and evaluation processes (Liou & Kar 2014; Pedro-Monzonís *et al.* 2015; Numata *et al.* 2017; Talsma *et al.* 2018).

Many ET monitoring and estimation methods have emerged with related theoretical research. These include the water balance method, aerodynamics methods, and scintilla meter measurements (Bowen 1926; Thornthwaite 1948; Howell *et al.* 1991; Rana & Katerji 2000). These methods have displayed the ability to describe the characteristic rules of the ET processes at micro and farmland scales in detail. In addition, they have also provided important references and basic information for

water vapor exchanges on underlying surfaces, decision-making concerning farmland irrigation, comprehensive water resource management, and so forth (Long & Singh 2013; Liou & Kar 2014; French *et al.* 2015; Xu *et al.* 2015). However, in terms of regional ET estimation, owing to fluctuations in weather conditions and the dynamic nature of water-heat transfer processes (Gao *et al.* 2008), it has been determined that these traditional point-scale monitoring methods and approaches cannot fully reflect the actual characteristics of spatial changes in ET (Su *et al.* 2003; Cai *et al.* 2009; Monteith & Unsworth 2013; Taherparvar & Pirmoradian 2018). It has been determined that remote sensing technology can offer a new approach for regional ET estimation. Because of the spatial continuity and large span characteristics of remote sensing, the water that is consumed during ET can be derived directly, without the need to quantify other complex hydrological processes (Trezza *et al.* 2013).

ET models using remote sensing technology have been developed in recent years, including empirical methods and mechanism methods. Many achievements in theory innovation and method techniques have been presented (Khand *et al.* 2017a). Among these proposed methods, two-source energy balance (TSEB), surface energy balance index (SEBI), simplified surface energy balance index (S-SEBI), surface energy balance algorithm for land (SEBAL), mapping evapotranspiration at high resolution with internalised calibration (METRIC) model have been widely used to calculate regional ET based on the theory of energy balance (Menenti 1993; Norman *et al.* 1995; Bastiaanssen *et al.* 1998a; Roerink *et al.* 2000; Su 2002; Allen *et al.* 2007b; Yang *et al.* 2010). As a typical representative of estimating regional ET by using remote sensing, the METRIC model is a variant of the SEBAL model that implements the residual method to calculate regional ET (Spiliotopoulos *et al.* 2017; Zamani Losgedaragh & Rahimzadegan 2018). The METRIC model has been successfully used in many areas, as a physical model for high-precision estimation of regional ET (Allen *et al.* 2007a; Allen *et al.* 2013; Morton *et al.* 2013; Paço *et al.* 2014; Reyes-González *et al.* 2017; Spiliotopoulos *et al.* 2017).

The METRIC model is very similar to the SEBAL model (Zamani Losgedaragh & Rahimzadegan 2018), in which the computing core uses two limit pixels (dry and wet pixels) for solving the aerodynamic resistance and geothermic step above zero plane displacement. This method has been found to greatly increase the calculation efficiency of the sensible heat flux. However, the limit pixels which are subjectively chosen by the model users must be the upper and lower critical limits of the sensible heat flux/latent heat flux in the study area (Foolad *et al.* 2018), to ensure the calculation accuracy of the regional ET (Allen *et al.* 2007a, 2007b). During the previous practical application processes, different research studies tended to diversify the understanding of the underlying surface characteristics in study areas using inconsistent subjective selection criteria of the dry and wet limits. This resulted in the model's calculation accuracies being negatively influenced by the lack of ideal dry and wet pixel determinations (Allen *et al.* 2011a, 2011b, 2013), which then triggered space ambiguities in the estimations of the ET using remote sensing technology. For example, different research studies have used the same basic data and methods but obtained different ET estimation results. To address this problem, Tasumi and Khand suggested that the dry and wet limits should be selected according to the surface temperature (T_s) and leaf area index (LAI), or the normalized difference vegetation index (NDVI) related trend charts (Tasumi 2003; Khand *et al.* 2017b). Scientist established the dry and wet limit conditions for given pixels and periods by assuming the relatively stable energy differences between the dry and wet limits within certain periods (for example, daytime or eight day periods) (Scientist *et al.* 2013). Allen proposed that the dry and wet limits should be selected by CIMEC processes and based on setting the relative location conditions of the weather stations and farmlands in a study area (Allen *et al.* 2013). Related scholars have found that surface temperature has an important impact on evapotranspiration (Jiang *et al.* 2020; Hu *et al.* 2021). Similar research results also showed that LAI was one of the important influencing factors of evapotranspiration (Xue *et al.* 2020; Volik *et al.* 2021; Wang *et al.* 2021). For the grassland region with few meteorological stations, arid climate, and sparse vegetation, there are still few studies by relevant scholars and experts (Yu *et al.* 2020). In the process of understanding the METRIC model in similar situations, we have not found more scholars to explore the relevance. Therefore, we try to use a new dry-wet boundary method to verify and determine the corresponding dry-wet boundary.

In general, it is easy for researchers to make subjective errors when selecting sites independently. To some extent, the errors caused by personal factors are avoided based on actual T_s and LAI, and the selection is made from an objective perspective as far as possible. The objectives of this study were to identify the dry and wet limits in grassland areas by analyzing the spatial distribution characteristic relationship of T_s and LAI; the water vapor flux data obtained by an eddy covariance system and the crop water consumption data of an irrigation monitoring station calculated by the water balance method were used for evaluating and validating the ET estimation results using Landsat images and the METRIC model. On this basis, the

spatiotemporal distribution of the regional ET during the crop growth season of 2011 in different land cover types was studied using eight effective sunshine images of Landsat-5 and Landsat-7.

2. MATERIALS AND METHODS

2.1. Study area

The Xilin River Basin is a typical inland river basin in the Inner Mongolia typical steppe areas of China (Chen 2002). The basin, with an area of approximately 11,172 km^2 (115.53° – 117.25°E, 43.41° – 44.63°N), has a typical continental temperate semi-arid climate. In accordance with the statistical data of the Xilinhot Station detailed on the National Meteorological Data website, the multi-year (period 1971–2011) average precipitation, ET from the water surface, air temperature, and wind speed are 263.5 mm, 1,904 mm, 3 °C, and 3.4 m s^{-1}, respectively. The average precipitation gradually decreases from the southeast to northwest (Sheng 2017). The National Scientific Research Station of the Xilin Gol Grassland Ecosystem in Inner Mongolia (GES) and the irrigation monitoring station of the Institute of Water Resources for Pastoral Areas (IMS) are both located within the study area (Figure 1).

It was observed that the land cover in the study area included six types of arable land, forest land, grassland, water, urban land and unutilized land (Figure 1). The arable land mainly referred to the irrigated artificial grassland used for planting silage maize and a small amount of alfalfa. The crops were found to be influenced by climatic conditions, which generally resulted in a short growth season from May to September. The forest land was mainly distributed at the southern foothills of the Greater Khingan Mountains in the southeastern section of the study area. The grassland areas were the main land cover type in the study area, and accounted for more than 90% of the entire basin, which mainly included Stipa grandis and Chinensis (Bai *et al.* 2004; Li *et al.* 2016). The water areas mainly comprised the Xilin River, which was observed to transverse the entire basin. The unutilized land, such as bare and wetland areas, was mainly distributed on both sides of the river channels. Xilinhot City, which was located in the middle sections of the river basin, was the main urban land area.

2.2 Data

(1) Landsat data

In this study, Landsat-5 and Landsat-7 images were chosen to estimate ET. In the data bands of these images, visible light and near-infrared bands have a high spatial resolution of 30 m, which satisfies the validation requirements for the spatial accuracy of ET estimation results in this study. In combination with the cloud cover of the study area, the data were divided into a calibration period and a verification period. The effective 8-day sunshine data during the crop growth season from 2006 to 2009 were used to study the selection scheme of the dry and wet pixels in the METRIC model, and the effective 8-day

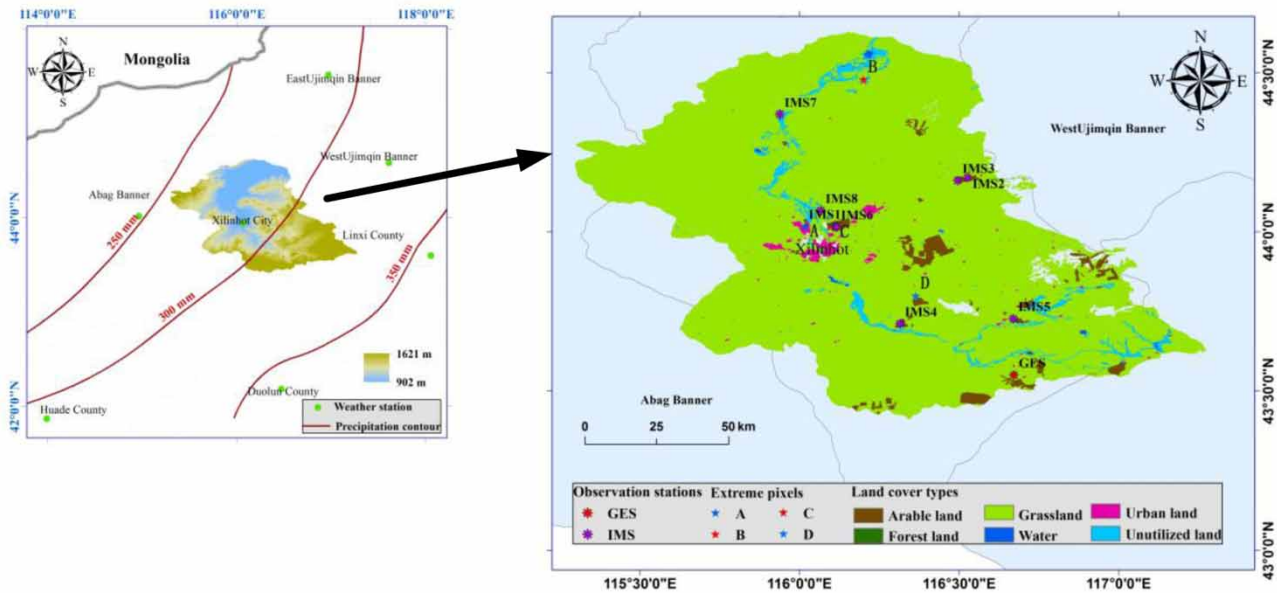

Figure 1 | Study area location.

sunshine data during the crop growth season (from May to September) of 2011 (day of the year from 121 to 273) were used to calculate the long-time scale of ET (Table 1). All the data were obtained from the United States Geological Survey (http://glovis.usgs.gov/).

(2) Meteorological data

Meteorological data included air temperature, wind velocity, water vapor pressure, solar radiation, humidity, and precipitation in the seven weather stations of East Ujimqin Banner, Abag Banner, Huade County, West Ujimqin Banner, Xilinhot City, Linxi County, and Duolun County (Figure 1). Among these, the air temperature data were used to calculate the surface temperature and net radiation by the METRIC model; the wind velocity data to calculate the aerodynamic resistance by the METRIC model; and the water vapor pressure data to calculate atmospheric transmittance and surface albedo by the METRIC model (Bastiaanssen *et al.* 1998a; Allen *et al.* 2007a). Other parameters such as solar radiation and humidity were used to calculate reference crop evapotranspiration (ET_0) by FAO Penman-Monteith equation (Allen *et al.* 1998). The meteorological data were obtained from the National Meteorological Data Information Center (http://data.cma.cn/).

(3) Evapotranspiration measurement data

The ET measurement data were obtained from an eddy covariance system in GES, and the eight irrigation monitoring stations (IMS) (Figure 1). (a). An eddy covariance system was an open system composed of a CSAT-3 three-dimensional ultrasonic anemometer and a LI7500 infrared analyzer. (b). The crop cultivated in the monitoring station was silage maize. The average volumetric weight of soil was 1.54–1.82 g cm-3 for a thickness varying from 0 to 100 cm. The field water holding capacity (θ_f) was 14.3%–19.0% (accounting for the dry soil weight), and the buried depth of the groundwater level was over 3 m. Based on the water balance method, the water consumption data of the silage maize growth period were calculated to evaluate the results of the METRIC model.

2.3. Theoretical basis

2.3.1. METRIC model

The SEBAL model is the theoretical basis of the METRIC model (Bastiaanssen *et al.* 1998a, 1998b; Allen *et al.* 2007b). In the model, by considering the interference of the underlying surface elevation, slope gradient, slope direction, and other factors, the surface information obtained through remote sensing are converted to surface albedo, surface emissivity, vegetation index, roughness length, surface temperature, and other characteristic parameters. This model is combined with the meteorological observational data of the underlying surfaces to calculate the regional ET (Allen *et al.* 2007b; González-Dugo *et al.* 2012). The theoretical equation is given as follows:

$$LE = R_n - G - H \tag{1}$$

where LE is the latent energy consumed by ET; R_n is the net radiation; G is the soil heat flux; and H is the sensible heat flux. Each energy component is generally expressed in W m^{-2}.

Table 1 | Landsat-5/7 TM data information (PATH 124/ROW 29 and 30)

Calibration period				Verification period			
date	day of the year (DOY_s)	cloud coverage	sensor	date	day of the year (DOY)	cloud coverage	sensor
2006/8/4	216	0%	Landsat-5	2011/4/12	102	1%	Landsat-5
2006/9/21	264	0%	Landsat-5	2011/5/14	134	8%	Landsat-5
2007/4/17	107	14%	Landsat-5	2011/5/22	142	23%	Landsat-7
2007/7/6	187	0%	Landsat-5	2011/8/2	214	0%	Landsat-5
2008/8/25	238	0%	Landsat-5	2011/8/10	222	0%	Landsat-7
2008/9/26	270	0%	Landsat-5	2011/9/11	254	0%	Landsat-7
2009/6/25	176	6%	Landsat-5	2011/9/19	262	2%	Landsat-5
2009/8/12	224	0%	Landsat-5	2011/10/5	278	6%	Landsat-5

(1) Net radiation

R_n denotes the difference in the whole-band radiation quantity between the downward projection from the sky (including the sun and the atmosphere) and the upward projection from the Earth's surface (including soil, plants, and water). This parameter represents the main power source for the energy and water transmission of the underlying surfaces (Allen *et al.* 2007b):

$$R_n = (1-\alpha)K_{in} + (L_{in} - L_{out}) - (1-\varepsilon)L_{in} \tag{2}$$

where α is the surface albedo (dimensionless); K_{in} is the incoming short-wave radiation (W m^{-2}); L_{in} is the incoming long-wave radiation (W m^{-2}); L_{out} is the outgoing long-wave radiation (W m^{-2}); and ε is the broad-band surface emissivity (dimensionless).

(2) Soil heat flux

G refers to the part of the energy stored in vegetation and soil due to conduction, and its changes are mainly affected by net radiation, surface temperature, and the vegetation cover on underlying surfaces. For the comprehensive analysis in this study, the achievements of Wright and Bastiaanssen are referred as follows (Wright 1982; Bastiaanssen *et al.* 1998a):

$$G = \frac{T_s - 273.15}{\alpha}(0.0038\alpha + 0.0074\alpha^2) \times (1 - 0.978NDVI^4)R_n \tag{3}$$

where T_s is the surface temperature (K); and NDVI is the normalized difference vegetation index (dimensionless).

(3) Sensible heat flux

H is a parameter describing the exchange of energy between land surfaces and atmosphere, in which energy is transferred from the Earth's surface to the atmosphere through convection or conduction. The calculation of H in the METRIC model is based on the following assumptions: dry and wet pixels exist in the study area. There is a linear relationship between the temperature difference dT ($dT = T_1 - T_2$) at z_1 and z_2 above the height of the zero-plane displacement and T_s. The space interpolation of the meteorological data on the underlying surfaces can then be avoided. Furthermore, the errors due to T_s are corrected to calibrate the calculation results of each pixel in remote sensing imaging through the elevation, slope gradient, and slope direction:

$$H = \rho_{air} c_p \frac{dT}{r_a} \tag{4}$$

where ρ_{air} is the air density (kg m^{-3}); c_p is the air specific heat capacity at a constant pressure (1,004 J kg^{-1} K^{-1}); and r_a is the aerodynamic resistance between two near-surface heights, which has been calculated by the Monin–Obukhov theory (Allen *et al.* 2007b). The calculation equations are given as follows:

$$dT = aT_{s,adtum} + b \tag{5}$$

$$T_{s,adtum} = T_s + 0.0065\Delta Z \tag{6}$$

where a and b are empirical constants; $T_{s,adtum}$ is the surface temperature adjusted to a common elevation data for each image pixel by using a digital elevation model and customized lapse rate (K); for non-planar areas, it is necessary to use the numerical elevation difference ΔZ for the corrections; and ΔZ is the difference between the elevation of each pixel and the reference elevation (m).

Dry and wet pixels are the two extreme pixels required for calculation using the METRIC model. Dry pixels refer to the dry idle wasteland or bare land areas without vegetation cover; these pixels are characterized by high temperature and almost zero ET (Bastiaanssen *et al.* 1998a; Allen *et al.* 2007b). In this study, dry pixels approximately satisfied LE ≈ 0. The dry end of the dT function is estimated by rearranging (Equation (4)) for a selected dry pixel in the image:

$$dT_{dry} = \frac{(R_n - G)_{dry} r_{adry}}{\rho_{airdry} c_p} \tag{7}$$

where $r_{a\ dry}$ is r_a computed for the roughness and stability conditions of the dry pixel; and $\rho_{air\ dry}$ is ρ_{air} calculated at the dry pixel.

Wet pixels refer to areas with adequate water supply, dense vegetation growth, low temperatures and potential ET levels in the remote sensing images (Bastiaanssen *et al.* 1998a; Allen *et al.* 2007b). These could include completely covered areas or open water masses with good plant growth. For the wet pixels, $H \approx 0$ is usually set in the SEBAL model, and such H values are considered in the METRIC model (Allen *et al.* 2007b).

$$dT_{wet} = \frac{(R_n - G - H)_{wet} r_{awet}}{\rho_{airwet} c_p} \tag{8}$$

where $r_{a\ wet}$ is ra computed for the roughness and stability conditions of the wet pixel; $\rho_{air\ wet}$ is ρ_{air} calculated at the wet pixel.

The distribution of dT is obtained by extracting the information regarding the dry and wet pixels (Daniel *et al.* 2017). The values for a and b in (Equation (5)) are estimated from these two pairs of dT and associated $T_{s,adtum}$.

$$a = \frac{dT_{dry} - dT_{wet}}{T_{s,adtum,dry} - T_{s,adtum,wet}} \tag{9}$$

$$b = dT_{dry} - aT_{s,adtum,dry} \tag{10}$$

(4) Surface parameters

Surface parameters contain α, ε, NDVI, T_s and momentum roughness length (Z_{om}) which are crucial in the atmospheric-surface interaction and consequently affect the ET estimation. Among them, α is computed by integrating band reflectance within the short-wave spectrum using a weighting function (Allen *et al.* 2007b); ε is computed using an empirical equation (Tasumi 2003); NDVI is the ratio of the differences in reflectivity for the near-infrared band and red band to their sum (Allen *et al.* 2007b); T_s is the single window algorithm proposed by Qin (Qin *et al.* 2010); Z_{om} for each image is specified by the corresponding NDVI (Allen *et al.* 2007b).

(5) Long-time scale of the daily evapotranspiration

In addition, it is assumed that the instantaneous ET ratio (EF_{inst}, $EF_{inst} = \mathrm{LE_{inst}}/(R_n\text{-}G)\mathrm{inst}$) is equal to the daily ET ratio (EF_d, $EF_d = \mathrm{LE_d}/(R_n\text{-}G)_\mathrm{d}$), when the instantaneous ET is used to calculate the daily ET ($\mathrm{ET_d}$) (Bastiaanssen *et al.* 1998a, 1998b). In this study, to estimate long-time scale of the daily ET, the daily reference ET ratio ($\mathrm{ET_rF}$ is the ratio between $\mathrm{ET_d}$ and daily $\mathrm{ET_0}$, $\mathrm{ET_rF} = \mathrm{ET_d}/\mathrm{ET_0}$) of the eight $\mathrm{DOY_s}$ were calculated, and the crop growth season was divided into seven intervals (Table 1). Each interval consisted of two $\mathrm{DOY_s}$ of effective sunshine satellite images. Thereafter, by assuming that the $\mathrm{ET_rF}$ change between two adjacent effective sunshine days is linearly correlated with the DOY, interpolation was used to calculate the daily ET during the period:

$$ET_{d,DOY} = (c \times DOY + d) \times ET_{0,DOY} \tag{11}$$

$$c = \frac{ET_rF_n - ET_rF_m}{DOY_n - DOY_m} \tag{12}$$

$$d = ET_rF_n - c \times DOY_n \tag{13}$$

where c and d are constants; $\mathrm{ET_{d,DOY}}$ and $\mathrm{ET_{0,DOY}}$ are the daily ET and $\mathrm{ET_0}$ between two adjacent effective sunshine days respectively; and $\mathrm{ET_rF_n}$ and $\mathrm{ET_rF_m}$ are the $\mathrm{ET_rF}$ when the DOY is n and DOY is m, respectively (DOY_n: 278,262,254,222,214,142,134; DOY_m: 262,254,222,214,142,134,102).

A flow chart of the METRIC model is shown in Figure 2 (Chang *et al.* 2017).

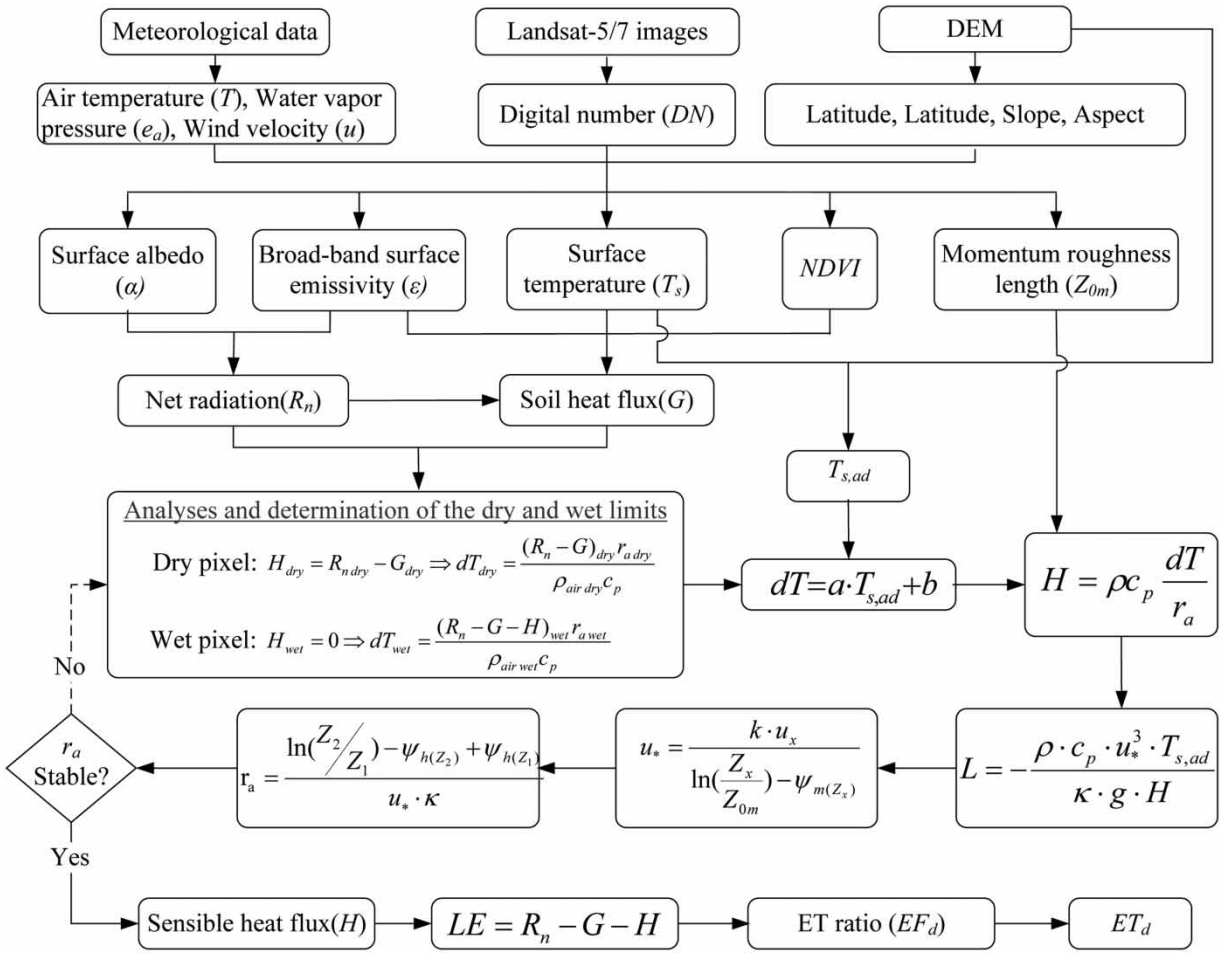

Figure 2 | Flowchart of the METRIC model. L is the Monin-Obukhov length, and ψ_m and ψ_h are the stability correction factors for momentum and sensible heat, respectively. Z is the elevation of each pixel (m). u_* is the friction velocity (m s^{-1}). κ is von Karman's constant (0.41).

2.3.2. Evapotranspiration of silage maize at irrigation monitoring stations

The evapotranspiration of silage maize consumed by the crops was calculated using the water balance method as follows (Kang 2007):

$$ET_{IMS}=P_a+I-L+K-\Delta W \tag{14}$$

where ET_{IMS} is the ET value of IMS; P_a is the effective precipitation; I denotes irrigation; L is the amount of deep leakage; and K is the groundwater recharge amount. Because the buried depth of the groundwater was greater than 3 m, as per the observations of a buried negative pressure meter, groundwater recharge was observed to be minimal; therefore, $K\approx 0$. ΔW represents the variation in planned soil moisture layer during the growth cycle of silage maize. All the above parameters are in units of mm.

The water balance equation can be used to calculate the water consumption of silage maize during the crop growth of the IMS. The result of this calculation is then used to verify the regional ET estimated by the METRIC model.

2.3.3. Comparison of ET_{METRIC} and ET_{IMS}

ET_{METRIC} was accurately estimated by computing the mean absolute error (MAE) and mean relative error (MRE).The values of MAE and MRE were computed as follows (Mayer & Butler 1993):

$$MAE=\frac{\sum_{i=1}^{t}|ET_{METRIC}-ET_{IMS}|}{t} \tag{15}$$

$$MRE = \frac{1}{t}\sum_{i=1}^{t}\left|\frac{ET_{METRIC} - ET_{IMS}}{ET_{IMS}}\right| \times 100\% \quad (16)$$

where ET_{METRIC} is the estimated ET by the METRIC model; and t is the number of observations.

3. RESULTS AND DISCUSSION

3.1. Analyses and determination of the dry and wet limits

The dry and wet limits in the METRIC model refer to the dry and wet pixels. Among these, the dry pixel refers to the dry idle wasteland or bare land areas without vegetation cover, and the pixels are characterized by high temperatures and almost zero ET (Bastiaanssen *et al.* 1998a; Allen *et al.* 2007b). In this study, the dry pixel approximately satisfied $H \approx R_n$-G, LE ≈ 0. The wet pixels refer to the pixels with adequate water supply, dense vegetation growth, low temperatures and potential ET levels in the remote sensing images. These could include completely covered areas or open water masses with good plant growth. For the wet pixels, $H \approx R_n$-G-LE, of which H ≈ 0 is usually set in the METRIC model. The distribution of the dT was obtained by extracting the information regarding the dry and wet pixels (Daniel *et al.* 2017). In the process of selecting dry and wet points, the image brought by underlying surface factors should be fully considered. The selection of dry and wet points should conform to the similar conditions of the surrounding environment to avoid the occurrence of other ground classes in the vicinity, so as to bring errors to the calculation results. Then, in order to reduce the ET estimation errors caused by spatial ambiguity in the extraction processes, for the typical steppe areas in the Xilin River Basin with the scarce meteorological station and sparse vegetation on the underlying surface, the identification scheme of this study was based on a spatial distribution feature relation graph of the T_s and LAI (Figure 3(a)). Then, by identifying the A, B, C and D limit pixels in the spatial distributions of the T_s and LAI, the different dry and wet pixel combination plans were set. The water vapor flux data measured by this study's eddy covariance system were used to evaluate the accuracy of the regional ET estimations of the different dry and wet pixel combinations, in order to further determine the dry and wet limit recognition scheme in the grasslands of the study area.

The recognition of the regional dry and wet pixels required the calculation of the T_s and LAI. Among these, a single-window algorithm was used to calculate the T_s that ranged between 280.31 and 312.09 K, with an average value of 302.67 K in the study area (Figure 4(a)). The soil regulatory vegetation index SAVI was applied to calculate LAI that ranged between 0.00 and 6.00, with an average value of 0.60 in the study area (Figure 4(b)) (Allen *et al.* 2007b). The T_s and LAI of 150 pixels were randomly extracted in this study. The A, B, C, and D points of the study area were determined in combination with the land coverage types (Figure 1). Among these, Point A was a bare land section in the study area, where the pixel type was mainly exposed and there was minimal vegetation. Point B was a wetland section in the study area. Point C was a farm-growing area, and the pixels in this area were artificially irrigated grassland with sufficient water. Point D was a dry

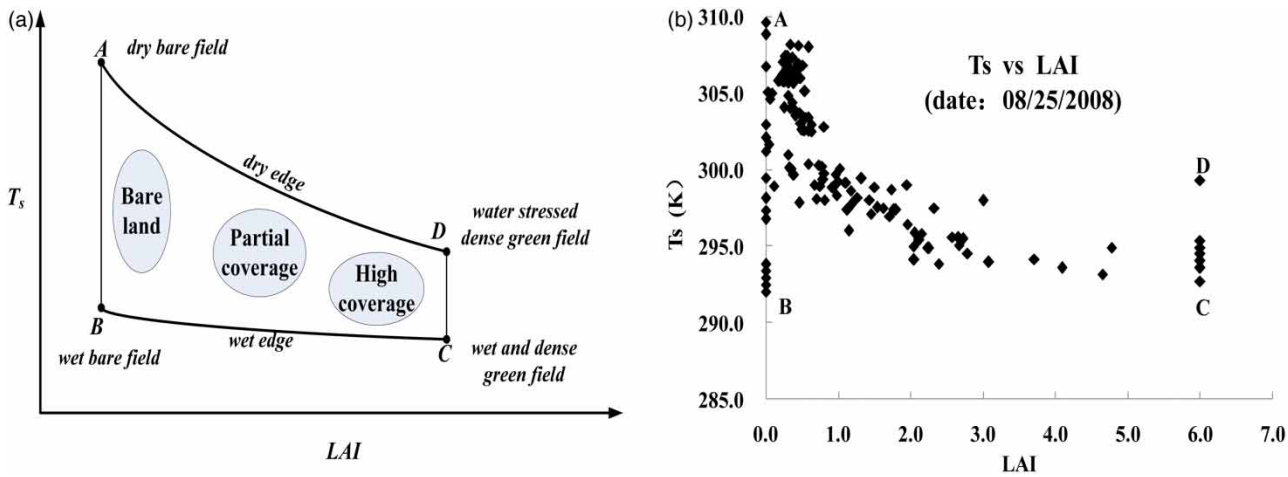

Figure 3 | General trend of surface temperature (T_s) and leaf area index (LAI).

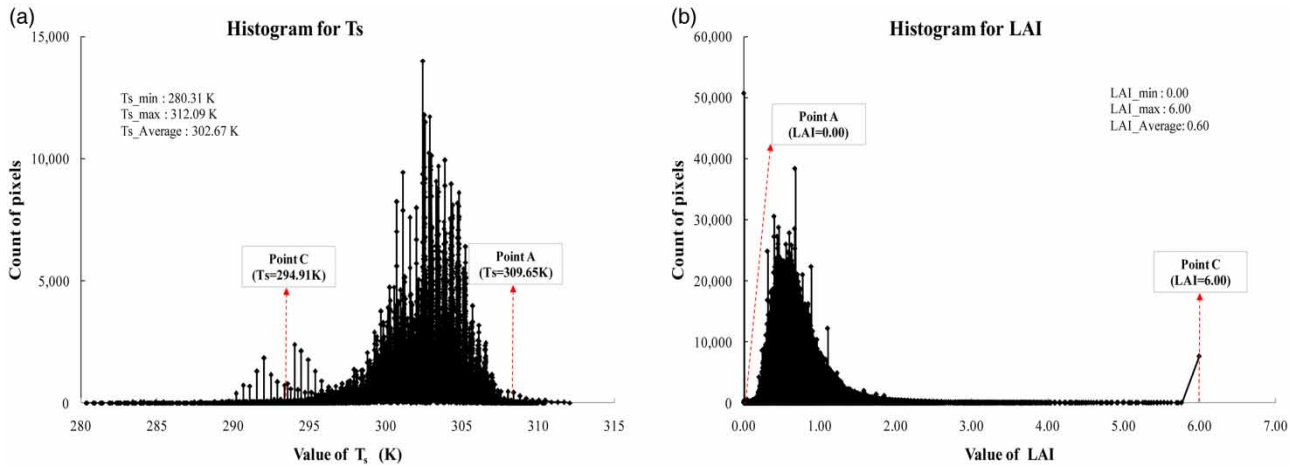

Figure 4 | Frequency histogram for surface temperature (T_s) and leaf area index (LAI).

agricultural field in the study area, where the dry agricultural land had high vegetation coverage due to the planting of crops. To test the influences of the different dry and wet limits on the estimation accuracy of the H and LE, and in accordance with the T_s-LAI related trend chart of the study area (Figure 3(b)), four dry and wet limit combinations $M_{dry,wet}$ were set ($M_{A,B}$;$M_{A,C}$; $M_{D,B}$; and $M_{D,C}$). Then, H, LE and basin ET on the satellite crossing day were calculated (Table 2).

Table 2 details the basin ET results which were calculated by the METRIC model on August 25, 2008. When compared with the measured data of the water vapor flux in the eddy covariance system of the GES, and under the premise of constant characteristic parameters and other energy components, the METRIC model's estimates of the regional ET results of four dry and wet limit combinations displayed major differences. Among the four combinations, the ET estimation results of $M_{A,C}$ were determined to be the most ideal. The daily ET estimation results ($ET_{d,METRIC}$) had a relative error of 9.2% with the measured data of water vapor flux by the eddy covariance system ($ET_{d,GES}$), followed by the $M_{A,B}$ combination with a relative error of 27.7%. The results of the $M_{D,B}$ and $M_{D,C}$ combinations were found to have the poorest estimation accuracies, with relative errors of approximately 100%. It was found that when the constraint of the ET was considered to be greater than 0, $ET_{d,METRIC} \approx 0$ was estimated by the two combinations. The reasons for these results were that in the two combinations of $M_{A,C}$ and $M_{A,C}$ with Point D as the dry pixel, and the mean value of the stable H was greater than (R_n-G) through the Monin-Obukhov similarity theory, which led to an unreasonable phenomenon of LE. In conclusion, the $M_{A,C}$ combination formed by Points A and C was determined to be a more suitable selection as the dry and wet pixels in the study area.

The calculation results revealed that the T_s of the dry pixels (Point A) were distributed in the front 5% of the frequency histogram, and those of the wet pixels (Point C) were distributed in the rear 5% of the frequency histogram (Figure 4(a)).

Table 2 | Effects of the different dry and wet limit combinations on the ET estimation

$M_{dry,wet}$	$T_{s,adtum,dry}$ $T_{s,adtum,wet}$ K	LAI_{dry} LAI_{wet} /	$(R_n\text{-}G)_{dry}$ $(R_n\text{-}G)_{wet}$ W m^{-2}	a /	b /	H^* W m^{-2}	$(R_n\text{-}G)^*$ W m^{-2}	$ET_{d,METRIC}$ mm d^{-1}	$ET_{d,GES}$ mm d^{-1}	Relative error %
$M_{A,B}$	309.65 291.09	0 0	355.72 411.23	0.56	− 159.8	261.69	396.17	3.13	4.32	28%
$M_{A,C}$	309.65 294.91	0 6	355.72 480.21	0.74	− 215.61	222.36	396.17	3.93	4.32	9%
$M_{D,B}$	299.28 291.09	6 0	449.53 411.23	1.12	− 323.14	939.76	396.17	≈ 0	4.32	100%
$M_{D,C}$	299.28 294.91	6 6	449.53 480.21	2.17	− 635.87	759.58	396.17	≈ 0	4.32	100%

Note: ① *a* and *b* are empirically determined constants from the dT calculation for a given satellite image. ② * is mean data of all of the image pixels when using dry and wet limits combinations.

According to this study's calculation results, the LAI of the dry pixels (Point A) were distributed in the rear 3% of the frequency histogram, and those of the wet pixels (Point C) were distributed in the front 3% of the frequency histogram (Figure 4(b)). Based on the comprehensive consideration of the land cover status on the underlying surfaces of the study area, the high-temperature areas which accounted for the front 5% of the T_s frequency histogram, and the bare land which accounted for the rear 1–3% of the LAI frequency histogram, were selected as the dry pixels in this study. The low-temperature areas which accounted for the rear 5% of the T_s frequency histogram, and the farmland which accounted for the front 1–3% of the LAI frequency histogram, were selected as the wet pixels. The specific operational steps were as follows: With the land cover as the base map, GIS was used to overlap the T_s and LAI land areas. Then, in accordance with the set constraints of the above-mentioned scheme, GIS or ENVI software were used to automatically identify the dry and wet pixels (the percentage was the data with invalid values eliminated according to the season and cloud cover).

3.2. Analysis of the ET in the calibration period

The results of the regional ET estimated by the dry and wet limits identification scheme need to be verified and analyzed in order to determine if the characteristics of the ET and water consumption on the underlying surfaces had been accurately reflected. In previous related studies, it had been determined that the eddy covariance system of GES was one of the most reliable means to monitor ET (Siedlecki *et al.* 2016; Consoli *et al.* 2018). Therefore, it was utilized to measure water vapor flux data in order to evaluate the accuracy of the estimated calibration period of this study's METRIC model (Table 3).

$ET_{d,METRIC}$ and $ET_{d,GES}$ of the natural grassland areas with flat terrain and uniform growth in the study area during eight different DOY_s are presented in Table 3. The $ET_{d,METRIC}$ was combined with field survey results, land cover status and the NDVI feature analysis, in order to extract the average ET of nine pixels (0.81 ha) within a 3×3 window centered on the location of the eddy covariance system. The $ET_{d,\ GES}$ was the actual measurement of the water consumption data by the water vapor flux of the GES. It was found that, when compared with the measured $ET_{d,GES}$, the absolute error of the eight DOY_s of the $ET_{d,METRIC}$ ranged between −0.02 and 0.60 mm/d, with an average value of 0.17 mm/d. The relative error was determined to be between 4.0 and 37.9%, with $MRE = 18.8\%$. Meanwhile, it was found that among the eight DOY_s, the 6-day $ET_{d,METRIC}$ results were higher than the measured data of the $ET_{d,GES}$. Therefore, when combined with the conclusion that the eddy covariance method often underestimates the ET (due to the unclosed energy balance equation obtained by Massman (Massman & Lee 2002)), it was considered in this study that the daily ET results of the natural grassland areas simulated by the METRIC model were acceptable.

In addition, linear regression was conducted on the ET simulated using this study's METRIC model, as well as the ET measured by the eddy covariance system (Figure 5). As viewed from the results, the simulated and measured values displayed relatively high goodness of fit. The determinant R^2 of the regression equation was determined to be 0.96, and the RMSE was 0.32 mm/d, which was considered to be a high fitting degree. In addition, the slope of the linear equation was 0.94, which was close to the standard value of 1.0. The ET values estimated by the METRIC model were observed to be consistent with the actual measured data of the eddy covariance system in the overall change trend.

Table 3 | Comparisons of the ET values observed by eddy covariance with those estimated using METRIC for different periods on nature grassland in GES

date	day of the year (DOY)	$ET_{d,GES}$ (mm d^{-1})	$ET_{d,\ METRIC}$ (mm d^{-1})	Absolute error (mm)	Relative error (%)
2006/8/4	216	1.45	1.72	0.27	18.7
2006/9/21	264	1.18	1.41	0.22	18.9
2007/4/17	107	0.66	0.90	0.25	37.9
2007/7/6	187	1.07	1.36	0.29	27.0
2008/8/25	238	4.32	3.93	−0.40	9.2
2008/9/26	270	0.53	0.51	−0.02	4.0
2009/6/25	176	3.22	3.82	0.60	18.7
2009/8/12	224	0.82	0.95	0.13	16.2

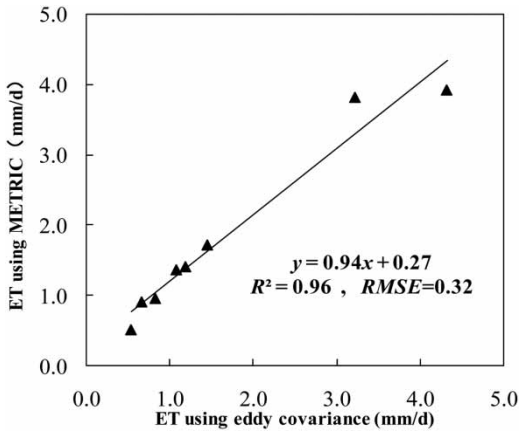

Figure 5 | The fitted line of the ET estimated by the METRIC model and the ET measured by the eddy covariance system.

3.3. Estimated accuracy of evapotranspiration by METRIC model

All the crops grown at the eight monitoring stations were silage maize, with an average growth period of 97 days. The irrigation methods included central pivot sprinkler irrigation (CPSI), drip irrigation (DI), low-pressure pipeline irrigation (LPPI), and semi-fixed irrigation (SFI). The average actual water consumption of silage maize during the growth period was determined to be 443.20 mm using (Equation (14)). The average value of ET_{METRIC} of silage maize in the eight stations during the growth period was determined to be 428.73 mm, in which MAE = 49.15 mm and MRE = 11.1%. By summarizing the previous research results, Kalma reviewed the various estimation methods of different remote sensing ET, and observed that when compared with the ground-based ET measurement value, the majority of the relative errors ranged from 15.0% to 30.0% (Kalma *et al.* 2008). Therefore, in this study it was believed that the accuracy of long-term scale ET estimation was reasonable and consistent with the previous research related conclusions (Allen *et al.* 2011b; Lian & Huang 2015) (Table 2).

The estimation results summarized in Table 4 show that the MRE of CPSI and DI is lower than that of SFI and LPPI by approximately 21.5% and the cause of this phenomenon was analyzed in this study. The ET_{METRIC} is the regional comprehensive water consumption of the underlying surface. Within the corresponding time period, the researchers randomly sampled the field water consumption data, and CPSI and DI was employed to reflect the actual situation of field water consumption more objectively than SFI and LPPI, because historical measured data are applied to confirm that the uniformity of CPSI and DI is better than that of SFI and LPPI. Therefore, ET_{IMS} by SFI and LPPI may not accurately reflect the regional comprehensive water consumption as CPSI and DI do.

3.4. Spatial characteristic of the ET

The spatial distribution of the ET in the Xilin River Basin during the crop growth season ranged from 62.31 to 778.86 mm, with an average value of 461.51 mm, and an average daily ET intensity of 3.02 mm/d (Figure 6). In terms of the spatial

Table 4 | Comparison of ET_{METRIC} and ET_{IMS} during the growth period of silage maize

No.	Irrigation type	Growth cycle (DOY_m-DOY_n)	P_a (mm)	I (mm)	L (mm)	ΔW (mm)	ET_{IMS} (mm)	ET_{METRIC} (mm)	Absolute error (mm)	Relative error (%)
IMS1	CPSI	140–243	133.40	450.00	/	36.38	547.03	511.26	35.77	6.5
IMS2	CPSI	145–243	127.30	337.50	/	5.28	459.52	470.32	10.80	2.3
IMS3	CPSI	145–243	127.30	375.00	/	35.48	466.83	490.83	24.00	5.1
IMS4	CPSI	152–243	127.30	405.00	/	33.62	498.69	469.55	29.14	5.8
IMS5	CPSI	152–243	127.30	375.00	/	41.00	461.31	479.02	17.72	3.8
IMS6	DI	156–250	127.30	142.00	1.73	− 10.54	278.11	308.53	30.42	10.9
IMS7	LPPI	145–243	127.3	120	/	− 8.46	255.76	311.47	55.71	21.8
IMS8	SFI	145–243	127.3	450	/	− 1.26	578.56	388.86	189.7	32.8

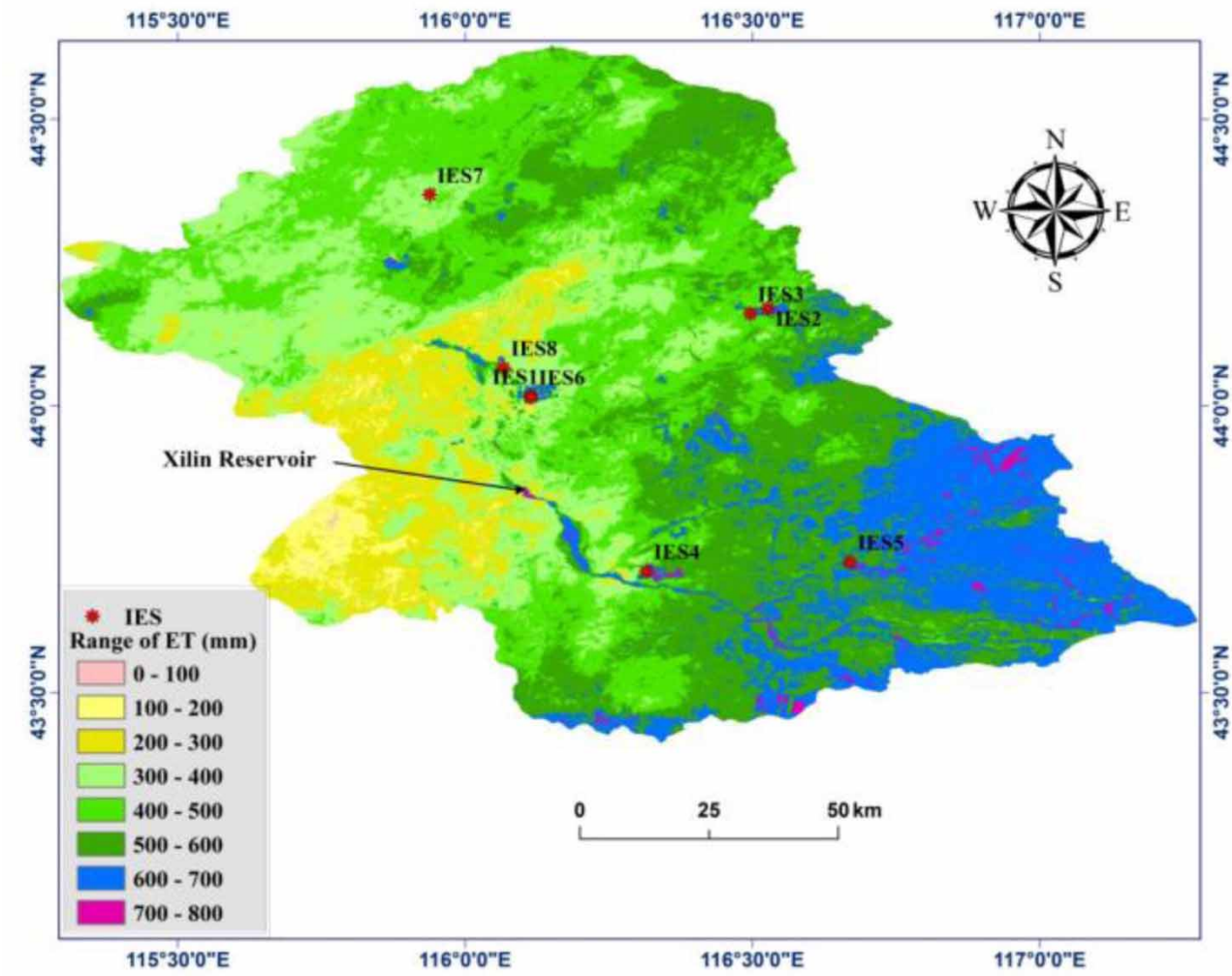

Figure 6 | Estimating the ET value of crop growth season by the METRIC model.

distribution, the ET displayed obvious spatial distribution traits from the forest-grass land intersections in the southeastern section of the Xilin River Basin, to the low-covered grassland areas in the northwestern section. These traits were found to be due to the comprehensive influences of climatic conditions, soil moisture supply status, vegetation cover, and other factors. In this study, based on the analysis of the ET results detailed in Figure 6 and land cover types detailed in Figure 1, it was found that except for the water masses with high ET characteristics (such as the Xilin Reservoir), the ET during the crop growth season displayed an overall declining change trend from the southeast to the northwest. The southeastern part of the basin was a shrubby forest area at the southern foot of the Great Khingan Mountains. This area was characterized by relatively abundant rainfall, favorable growth of forest-grass vegetation, and good ET conditions. Moreover, in recent years, the small amount of natural grassland in the basin has developed to become irrigated artificial grassland for silage maize cultivation. As a result, the ET of the forest-grass land intersections, and the irrigated artificial grassland planting areas in the southeast, was observed to be somewhat higher than that in the western and northern natural grass areas of the basin.

The ET of crop growth season was extracted according to the vegetation cover classification. For the different land cover types, the sequence was as follows: $ET_{water} > ET_{arable\ land} > ET_{forest\ land} > ET_{unutilized\ land} > ET_{grassland} > ET_{urban\ land}$ (Figure 7). The sufficient water levels had created favorable ET conditions for the water mass areas. During the crop growth season, the ET_{water} exceeded 740 mm (Figure 7(d)), and the average daily ET intensity reached 4.92 mm d^{-1}, which was the maximum among all the land types. In addition, a standard deviation of 7.28 mm indicated that the water masses were evenly distributed

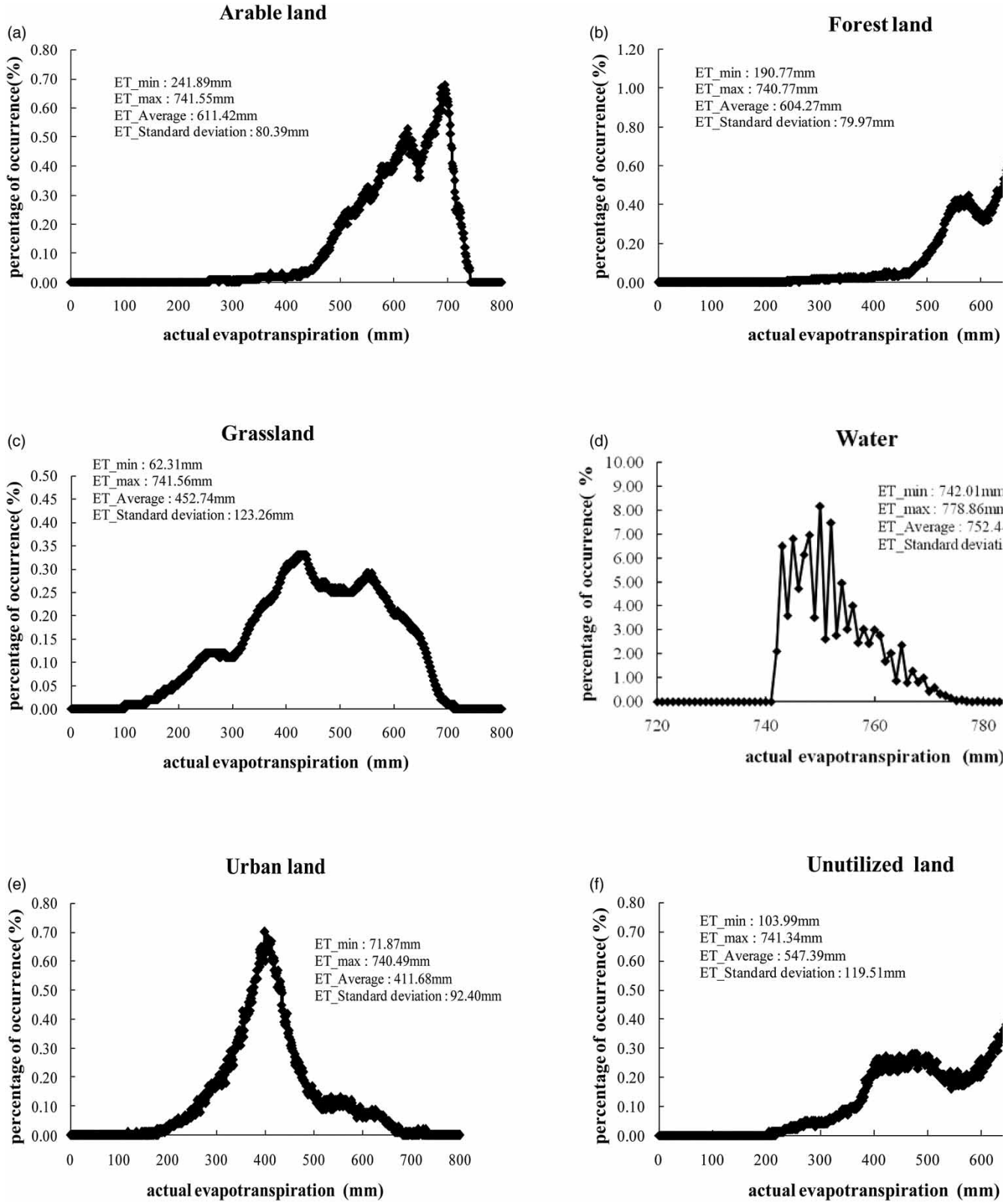

Figure 7 | Frequency distribution of the ET_{METRIC} values for different land cover types.

in space. The average ET value of the arable land in the basin was determined to be 611.42 mm (Figure 7(a)), and the average ET intensity was 4.00 mm d^{-1}. The artificially irrigated grasslands cultivated from the natural grasslands were supported by modern irrigation technology to ensure that the water demands for crop growth were met. The forest land was mostly distributed in the southeastern mountainous areas and characterized by abundant precipitation. The relatively sufficient precipitation and moist underlying surface environments guaranteed adequate water for plant growth, and the ET level was similar to that of hearable land (Figure 7(b)). The distribution of the unutilized land was mainly in the low-lying areas of the Xilin River Valley (Figure 1), as well as the exposed highlands along the coast. The average ET of the crop growth season was 547.39 mm. However, the mean variance calculation result of 119.51 mm indicated that the ET of the unutilized land in the regions was quite different (Figure 7(f)). According to the field investigations and previous research results, due to the precipitation reductions caused by climate change in the entire basin, especially in the western region (Wang *et al.* 2017), coupled with grassland degradation induced by overgrazing in recent years (Tong *et al.* 2004), some of the typical steppe areas have degenerated into desertification grassland or sandy land, with low vegetation coverage, drought, and little water. These factors jointly restrict the activities of the ET in grassland areas. The results showed that the ET intensity of the grassland (2.96 mm d^{-1}) was significantly lower than that of the majority of the other land types, and only higher than that of the urban land areas (2.69 mm d^{-1}) (Figure 7(c) and 7(e)).

4. CONCLUSIONS

The goal of this research study was to estimate the spatial and temporal distributions of the ET in typical steppe areas using a remote sensing energy balance method. In order to solve the spatial ambiguity problems of identifying the dry and wet limits in remote sensing ET estimations, the effects of the different dry and wet limit combinations on the ET estimation in typical steppe areas of the Xilin River Basin were estimated and compared based on Landsat images and the METRIC model. According to the test results of the water vapor flux data measured by an eddy covariance system, the error percentage of the ET in the eight DOY_s regions estimated by the dry and wet limit pixels and comprehensively selected from the T_s and LAI, was 18.8% on average. The simulated values were observed to have high goodness of fit with the measured values. On this basis, the spatiotemporal distribution of the regional ET during the crop growth season of 2011was studied using eight effective sunshine images of Landsat-5 and Landsat-7. The relative error was found to be 11.1%, which was verified by the measurement data in eight silage maize irrigation monitoring stations using the water balance method. Then, combined with the verification results of this study's eddy covariance system and water balance method, as well as the previous research conclusions of the regional ET estimated by remote sensing, a certain reliability was proven in the estimations of the ET of the typical steppe areas in the Xilin River Basin when Landsat images and the METRIC model were applied. Meanwhile, to analyze the spatial distributions of the ET, the ET results of the crop growth season were extracted according to the vegetation cover classification. It was concluded in this study that the spatial distribution of the ET of the different land cover types in the study area were as follows: $ET_{water} > ET_{arable\ land} > ET_{forest\ land} > ET_{unutilized\ land} > ET_{grassland} > ET_{urban\ land}$.

ACKNOWLEDGEMENTS

This work was supported by the special fund of China Institute of Water Resources and Hydropower Research (Grant NO. MK2020J03), the Natural Science Foundation of Inner Mongolia (Grant NO. 2020MS05057). The authors are grateful to the National scientific research station of Xilin Gol Grassland Ecosystem in Inner Mongolia for providing the eddy covariance data and meteorological data. We greatly appreciate the help of Chen shiping in providing ground-based measurements of evapotranspiration.

CONFLICT OF INTEREST STATEMENT

The authors declare no conflict of interest.

DATA AVAILABILITY STATEMENT

All relevant data are included in the paper or its Supplementary Information.

REFERENCES

Allen, R. G., Pereira, L. S., Raes, D. & Smith, M. 1998 Crop Evapotranspiration: Guidelines for Computing Crop Water Requirements. FAO Irrigation and Drainage Paper No. 56. FAO, 56.

Allen, R. G., Tasumi, M., Morse, A., Trezza, R., Wright James, L., Bastiaanssen, W., Kramber, W., Lorite, I. & Robison Clarence, W. 2007a Satellite-based energy balance for mapping evapotranspiration with internalized calibration (METRIC)–applications. *Journal of Irrigation and Drainage Engineering* **133** (4), 395–406.

Allen, R. G., Tasumi, M. & Trezza, R. 2007b Satellite-Based energy balance for mapping evapotranspiration with internalized calibration (METRIC)–Model. *Journal of Irrigation and Drainage Engineering* **133** (4), 380–394.

Allen, R. G., Irmak, A., Trezza, R., Hendrickx, J. M. H., Bastiaanssen, W. & Kjaersgaard, J. 2011a Satellite-based ET estimation in agriculture using SEBAL and METRIC. *Hydrological Processes* **25** (26), 4011–4027.

Allen, R. G., Pereira, L. S., Howell, T. A. & Jensen, M. E. 2011b Evapotranspiration information reporting: I. Factors governing measurement accuracy. *Agricultural Water Management* **98** (6), 899–920.

Allen R. G., Burnett, B., Kramber, W., Huntington, J., Kjaersgaard, J., Kilic, A., Kelly, C. & Trezza, R. 2013 Automated calibration of the METRIC-Landsat evapotranspiration process. *JAWRA Journal of the American Water Resources Association* **49** (3), 563–576.

Bai, Y., Han, X., Wu, J., Chen, Z. & Li, L. 2004 Ecosystem stability and compensatory effects in the Inner Mongolia grassland. *Nature* **431** (7005), 181–184.

Bastiaanssen, W. G. M., Menenti, M., Feddes, R. A. & Holtslag, A. A. M. 1998a The surface energy balance algorithm for land (SEBAL): part 1 formulation. *Journal of Hydrology* **212** (98), 801–811.

Bastiaanssen, W. G. M., Pelgrum, H., Wang, J., Ma, Y., Moreno, J. F., Roerink, G. J. & Wal, T. V. D. 1998b A remote sensing surface energy balance algorithm for land (SEBAL): part 2: validation. *Journal of Hydrology* **212** (1–4), 213–229.

Batnasan, N. 2003 Freshwater issues in Mongolia. In *Proceeding of the National Seminar on IRBM in Mongolia*, Ulaanbaatar.

Bowen, I. S. 1926 The ratio of heat losses by conduction and by evaporation from any water surface. *Physical Review* **27** (6), 779–787.

Bradley, R. S. 1999 Paleoclimatology: reconstructing climates of the quaternary. *Arctic Antarctic & Alpine Research* **3** (31), 329–332.

Cai, X., Xu, Z., Su, B. & Yu, W. 2009 Distributed simulation for regional evapotranspiration and verification by using remote sensing (in Chinese with English abstract). *Transactions of the Chinese Society of Agricultural Engineering* **25** (10), 154–160.

Chang, Y., Ding, Y., Zhao, Q. & Zhang, S. 2017 Remote estimation of terrestrial evapotranspiration by Landsat 5 TM and the SEBAL model in cold and high-altitude regions: a case study of the upper reach of the Shule River Basin, China. *Hydrological Processes* **31** (3), 514–524.

Chen, S. 2002 *Study the Land use/Land Cover Change and Cycle of Xilin River Basin by Remote Sensing and GIS (in Chinese)*. University of Chinese Academy of Sciences (the Institute of Remote Sensing Applications), Beijing.

Consoli, S., Milani, M., Cirelli, G., Barbagallo, S., Marzo, A., Vanella, D. & Toscano, A. 2018 Energy and water balance of a treatment wetland under Mediterranean climatic conditions. *Ecological Engineering* **116**, 52–60.

Daniel, D. L. F., Ortegafarías, S., Fonseca, D., Ortegasalazar, S., Kilic, A. & Allen, R. 2017 Calibration of METRIC model to estimate energy balance over a drip-irrigated apple orchard. *Remote Sensing* **9** (7), 670.

Foolad, F. , Blankenau, P., Kilic, A., Allen, R. G., Huntington, J. L., Erickson, T. A., Ozturk, D., Morton, C. G., Ortega, S., Ratcliffe, I., Franz, T. E., Thau, D., Moore, R., Gorelick, N., Kamble, B., Revelle, P., Trezza, R., Zhao, W. & Robison, C. W. 2018 Comparison of the Automatically Calibrated Google Evapotranspiration Application–EEFlux and the Manually Calibrated METRIC Application. Preprints, 2018070040.

French, A. N., Hunsaker, D. J. & Thorp, K. R. 2015 Remote sensing of evapotranspiration over cotton using the TSEB and METRIC energy balance models. *Remote Sensing of Environment* **158**, 281–294.

Gao, Y. C., Long, D. & Li, Z. L. 2008 Estimation of daily actual evapotranspiration from remotely sensed data under complex terrain over the upper Chao river basin in North China. *International Journal of Remote Sensing* **29** (11), 3295–3315.

González-Dugo, M., Gonzalez-Piqueras, J., Campos, I., Balbontín, C. & Calera, A. 2012 Estimation of surface energy fluxes in vineyard using field measurements of canopy and soil temperature. *IAHS-AISH Publication* **352**, 59–62.

Howell, T. A., Schneider, A. D. & Jensen, M. E. 1991 History of Lysimeter Design and Use for Evapotranspiration Measurements, Lysimeters for Evapotranspiration and Environmental Measurements, pp. 1–9.

Hu, X., Shi, L., Lin, G. & Lin, L. 2021 Comparison of physical-based, data-driven and hybrid modeling approaches for evapotranspiration estimation. *Journal of Hydrology* **601**, 126592.

Jiang, Y., Tang, R. & Jiang, X. 2020 Assessing the directional effects of remotely sensed land surface temperature on evapotranspiration estimation. In: *IGARSS 2020–2020 IEEE International Geoscience and Remote Sensing Symposium*. pp. 4558–4561.

Kalma, J. D., Mcvicar, T. R. & Mccabe, M. F. 2008 Estimating land surface evaporation: a review of methods using remotely sensed surface temperature data. *Surveys in Geophysics* **29** (4–5), 421–469.

Kang, S. Z. 2007 *Conspectus of Agricultural Soil and Water Engineering* (in Chinese). Chinese Agricultural Press, Beijing, pp. 86–89.

Khand, K., Kjaersgaard, J., Hay, C. & Jia, X. 2017a Estimating impacts of agricultural subsurface drainage on evapotranspiration using the Landsat imagery-based METRIC model. *Hydrology* **4** (4), 1–16.

Khand, K., Numata, I., Kjaersgaard, J. & Vourlitis, G. L. 2017b Dry season evapotranspiration dynamics over human-impacted landscapes in the southern Amazon using the Landsat-based METRIC model. *Remote Sensing* **9** (7), 706.

Li, F., Zheng, J., Wang, H., Luo, J., Zhao, Y. & Zhao, R. 2016 Mapping grazing intensity using remote sensing in the Xilingol steppe region, Inner Mongolia, China. *Remote Sensing Letters* **7** (4), 328–337.

Lian, J. & Huang, M. 2015 Evapotranspiration estimation for an Oasis area in the Heihe River Basin using Landsat-8 images and the METRIC model. *Water Resources Management* **29** (14), 5157–5170.

Liou, Y.-A. & Kar, K. S. 2014 Evapotranspiration estimation with remote sensing and various surface energy balance algorithms – a review. *Energies* **7** (5), 2821.

Long, D. & Singh, V. P. 2013 Assessing the impact of end-member selection on the accuracy of satellite-based spatial variability models for actual evapotranspiration estimation. *Water Resources Research* **49** (5), 2601–2618.

Massman, W. J. & Lee, X. 2002 Eddy covariance flux corrections and uncertainties in long-term studies of carbon and energy exchanges. *Agricultural & Forest Meteorology* **113** (1–4), 121–144.

Mayer, D. G. & Butler, D. G. 1993 Statistical validation. *Ecological Modelling* **68** (1–2), 21–32.

Menenti, M. 1993 Parameteraization of land surface evaporation by means of location dependent potential evaporation and surface temperature range. Bolle, Feddes and Kalma, Exchange processes at the land surface for a range of space and time scales.

Monteith, J. L. & Unsworth, M. H. 2013 Chapter 8 - microclimatology of radiation: (iii) Interception by Plant Canopies and Animal Coats. In: *Principles of Environmental Physics (Fourth Edition)* (Monteith, J. L. & Unsworth, M. H., eds.). Academic Press, Boston, pp. 111–133.

Morton, C. G., Huntington, J. L., Pohll, G. M., Allen, R. G., McGwire, K. C. & Bassett, S. D. 2013 Assessing calibration uncertainty and automation for estimating evapotranspiration from agricultural areas using METRIC. *JAWRA Journal of the American Water Resources Association* **49** (3), 549–562.

Norman, J. M., Kustas, W. P. & Humes, K. S. 1995 Source approach for estimating soil and vegetation energy fluxes in observations of directional radiometric surface temperature. *Agricultural and Forest Meteorology* **77** (3–4), 263–293.

Numata, I., Khand, K., Kjaersgaard, J., Cochrane, M. & Silva, S. 2017 Evaluation of Landsat-based METRIC modeling to provide high-spatial resolution evapotranspiration estimates for Amazonian forests. *Remote Sensing* **9** (1), 46.

Paço, T. A., Pôças, I., Cunha, M., Silvestre, J. C., Santos, F. L., Paredes, P. & Pereira, L. S. 2014 Evapotranspiration and crop coefficients for a super intensive olive orchard. An application of SIMDualKc and METRIC models using ground and satellite observations. *Journal of Hydrology* **519**, 2067–2080.

Pedro-Monzonís, M., Solera, A., Ferrer, J., Estrela, T. & Paredes-Arquiola, J. 2015 A review of water scarcity and drought indexes in water resources planning and management. *Journal of Hydrology* **527**, 482–493.

Qin, Z., Karnieli, A. & Berliner, P. 2010 A mono-window algorithm for retrieving land surface temperature from Landsat TM data and its application to the Israel-Egypt border region. *International Journal of Remote Sensing* **22** (18), 3719–3746.

Rana, G. & Katerji, N. 2000 Measurement and estimation of actual evapotranspiration in the field under Mediterranean climate: a review. *European Journal of Agronomy* **13** (2–3), 125–153.

Reyes-González, A., Kjaersgaard, J., Trooien, T., Hay, C. & Ahiablame, L. 2017 Comparative analysis of METRIC model and atmometer methods for estimating actual evapotranspiration. *International Journal of Agronomy* **2017**, 1–16.

Roerink, G. J., Su, Z. & Menenti, M. 2000 S-SEBI: A simple remote sensing algorithm to estimate the surface energy balance. *Physics and Chemistry of the Earth, Part B: Hydrology, Oceans and Atmosphere* **25** (2), 147–157.

Scientist, G. B. S. P., Analyst, S. B. G., Scientist, R. K. S., Scientist, N. M. V. & Student, H. A. 2013 Operational evapotranspiration mapping using remote sensing and weather datasets: a new parameterization for the SSEB approach †. *Jawra Journal of the American Water Resources Association* **49** (3), 577–591.

Sheng, X. 2017 *Handbook of Characteristic Values of Rivers and Lakes in Inner Mongolia Autonomous Region (in Chinese). Xilinguole League*. Inner Mongolia University Press, Inner Mongolia, China, 248 pp.

Siedlecki, M., Pawlak, W., Fortuniak, K. & Zieliński, M. 2016 Wetland evapotranspiration: eddy covariance measurement in the Biebrza Valley, Poland. *Wetlands* **36** (6), 1055–1067.

Spiliotopoulos, M., Holden, N. M. & Loukas, A. 2017 Mapping evapotranspiration coefficients in a temperate maritime climate using the METRIC model and Landsat TM. *Water* **9** (1), 23.

Su, Z. 2002 The surface energy balance system (SEBS) for estimation of turbulent heat fluxes. *Hydrology & Earth System Sciences* **6** (1), 85–99.

Su, Z. , Yacob, A., Wen, J., Roerink, G., He, Y., Gao, B., Boogaard, H. & van Diepen, C. 2003 Assessing relative soil moisture with remote sensing data: theory, experimental validation, and application to drought monitoring over the North China Plain. *Physics and Chemistry of the Earth, Parts A/B/C* **28** (1–3), 89–101.

Taherparvar, M. & Pirmoradian, N. 2018 Estimation of rice evapotranspiration using reflective images of Landsat satellite in sefidrood irrigation and drainage network. *Rice Science* **25** (2), 111–116.

Talsma, C. J., Good, S. P., Jimenez, C., Martens, B., Fisher, J. B., Miralles, D. G., McCabe, M. F. & Purdy, A. J. 2018 Partitioning of evapotranspiration in remote sensing-based models. *Agricultural and Forest Meteorology* **260–261**, 131–143.

Tasumi, M. 2003 *Progress in Operational Estimation of Regional Evapotranspiration Using Satellite Imagery*.

Thornthwaite, C. W. 1948 An approach toward a rational classification of climate. *Geographical Review* **38** (1), 55–94.

Tong, C., Wu, J., Yong, S., Yang, J. & Yong, W. 2004 A landscape-scale assessment of steppe degradation in the Xilin River Basin, Inner Mongolia, China. *Journal of Arid Environments* **59** (1), 133–149.

Trezza, R., Allen, R. G. & Tasumi, M. 2013 Estimation of actual evapotranspiration along the Middle Rio Grande of New Mexico using MODIS and Landsat imagery with the METRIC model. *Remote Sensing* **5** (10), 5397–5423.

Volik, O., Kessel, E., Green, A., Petrone, R. & Price, J. 2021 Growing season evapotranspiration in boreal fens in the Athabasca oil sands region: variability and environmental controls. *Hydrological Processes* **35** (2), e14020.

Wang, H., Wang, J. H., Qin, D. Y. & Jia, Y. W. 2006 Theory and methodology of water resources assessment based on dualistic water cycle model (in Chinese with English abstract). *Journal of Hydraulic Engineering* **12**, 1496–1502.

Wang, J., Li, H. P., Lu, H. Y. & Li, J. 2017 Variation of precipitation and runoff in typical grassland area (in Chinese). *Journal of China Hydrology* **37** (04), 86–90.

Wang, L., Liu, Z., Guo, J., Wang, Y., Ma, J., Yu, S., Yu, P. & Xu, L. 2021 Estimate canopy transpiration in larch plantations via the interactions among reference evapotranspiration, leaf area index, and soil moisture. *Forest Ecology and Management* **481**, 118749.

Wright, J. L. 1982 New evapotranspiration crop coefficients. *Journal of the Irrigation & Drainage Division* **108** (IR2), 57–74.

Xu, D., Liu, Y., Yang, D. & Zhang, B. Z. 2015 *Evapotranspiration Scale Effect and Temporal-Spatial Scale Expansion (in Chinese)*. Science China Press, Beijing.

Xue, J., Bali, K. M., Light, S., Hessels, T. & Kisekka, I. 2020 Evaluation of remote sensing-based evapotranspiration models against surface renewal in almonds, tomatoes and maize. *Agricultural Water Management* **238**, 106228.

Yamanaka, T., Kaihotsu, I., Oyunbaatar, D. & Ganbold, T. 2007 Summertime soil hydrological cycle and surface energy balance on the Mongolian steppe. *Journal of Arid Environments* **69** (1), 65–79.

Yang, D., Chen, H. & Lei, H. 2010 Estimation of evapotranspiration using a remote sensing model over agricultural land in the North China Plain. *International Journal of Remote Sensing* **31** (14), 3783–3798.

Yu, D., Li, X., Cao, Q., Hao, R. & Qiao, J. 2020 Impacts of climate variability and landscape pattern change on evapotranspiration in a grassland landscape mosaic. *Hydrological Processes* **34** (4), 1035–1051.

Zamani Losgedaragh, S. & Rahimzadegan, M. 2018 Evaluation of SEBS, SEBAL, and METRIC models in estimation of the evaporation from the freshwater lakes (Case study: Amirkabir dam, Iran). *Journal of Hydrology* **561**, 523–531.

First received 26 August 2021; accepted in revised form 9 December 2021. Available online 30 December 2021